

Classical and quantum beam dynamics simulation of the RF photoinjector test bench

A.S. Dyatlov^{1,2,*}, A.V. Afanasyev², V.V. Kobets², A.E. Levichev³, M.V. Maksimov¹,
D.A. Nikiforov³, M.A. Nozdrin², K. Popov⁴, K.A. Sibiryakova³, K.E. Yunenko²,
D.V. Karlovets^{1, 5, †}

¹ *School of Physics and Engineering, ITMO University, 9 Lomonosova St.,
Saint-Petersburg, 191002, Russia*

² *Joint Institute for Nuclear Research, 6 Joliot-Curie St., Dubna, 141980, Moscow Region,
Russia*

³ *Budker Institute of Nuclear Physics, Siberian Branch of RAS, 11, Acad. Lavrentieva
Pr., Novosibirsk, 630090, Russia*

⁴ *Institute of Nuclear Physics, 1 Ibragimov Street, Almaty, 050032, Kazakhstan*

⁵ *Petersburg Nuclear Physics Institute of NRC "Kurchatov Institute", 1, mkr. Orlova
roshcha, Gatchina, Leningradskaya Oblast, 188300, Russia*

Abstract

We present beam-dynamics simulations for an S-band RF photoinjector test bench under development at the Joint Institute for Nuclear Research, aimed at producing high-quality electron beams and enabling future generation of relativistic vortex electrons with quantized orbital angular momentum (OAM). Simulations of the 1.5-cell photogun under the presently available RF gradient of 45 MV/m demonstrate stable bunch formation at low charge ($Q = 0.63$ pC), where space-charge forces are weak and the transverse emittance is dominated by RF-induced correlations. Optimization of the injection phase and cathode-region solenoid yields a robust emittance compensated regime with a final normalized emittance of $3.2 \pi \cdot \text{mm} \cdot \text{mrad}$. To assess prospects for accelerating vortex electron beams, we additionally model the quantum evolution of single-electron Laguerre–Gaussian wave packets. The results show that multi-MeV acceleration suppresses free-space spreading of the electron packet and preserves the packet’s initial OAM structure, indicating that the test bench provides suitable conditions for forthcoming experimental studies of relativistic vortex electrons.

1 Introduction

The generation of *relativistic vortex electron beams* – quantum states with a helical phase front and a quantized orbital angular momentum projection (OAM) – is attracting growing interest across accelerator, atomic, and nuclear physics, electron microscopy, quantum optics, and foundation of quantum mechanics [1, 2, 3, 4]. To date, vortex electrons have been generated only in the sub-MeV range, up to kinetic energies of ~ 300 keV of transmission electron microscopes [5, 6, 7]. Extending such structured states into the multi-MeV regime relevant for photoinjectors and linacs remains an outstanding challenge, yet promises significant impact, including new tools for nuclear and hadronic structure studies and potential alternatives to spin-polarized beams [4, 8, 9, 10].

It is important to distinguish the genuine vortex beams of single particles whose wave functions are characterized by a helical phase structure $\exp(i\ell\varphi)$ and a quantized OAM projection $\ell\hbar$ [2] from beams with modified transverse emittance ratios – such as flat and round beams demonstrated at

*email: aleksandr.dyatlov@metalab.ifmo.ru

†email: d.karlovets@gmail.com

Fermilab [11, 12, 13, 14]. These latter beams can possess a so-called *extrinsic* angular momentum, which is a property of the beam as a whole, so a quantum state of each particle in the beam is not defined, whereas the former quantum beams of single electrons possess the so-called *intrinsic* orbital angular momentum, the property of each electron, complementary to spin [2, 3, 4, 15].

One feasible route towards high-energy vortex electrons is the transfer of OAM from twisted ultraviolet light to electrons during photoemission [3, 16, 17]. Whereas the generation of pure vortex states with a definite angular momentum projection and its vanishing quantum uncertainty is challenging due the finite temperature, space-charge effects, and other factors [3, 15, 17], the generation of a superposition of vortex states with an uncertainty less than the mean OAM value of the beam seems feasible when the OAM is very high, in our case up to $\ell = 64\hbar$, and the bunch charge is low so the space-charge effects can be mitigated.

Realizing this mechanism requires a photoinjector capable of producing low-emittance beams with well-controlled transverse profiles and rapid acceleration, ensuring that the initial OAM-imprinted phase structure of the emitted electron is preserved during the early acceleration. To this end, a dedicated S-band RF photoinjector test bench is being developed at the Laboratory of Nuclear Problems, Joint Institute for Nuclear Research (JINR), combining a 1.5-cell RF gun [18] and a high-power UV laser system [19]. Along with relativistic vortex electrons, there are plans at the Institute of Modern Physics in China to put a twist on relativistic ions [10].

RF photoinjectors are widely used as high-brightness electron sources at facilities such as LCLS [20], the European XFEL [21], and SuperKEKB [22], owing to their ability to quickly suppress space-charge effects via high-gradient acceleration [23, 24]. At JINR, there exists a LINAC facility, which is a linear accelerator of electrons to the energy of 200 MeV and plans to come to 400 MeV in 2027 [25], it operates with a thermionic DC gun and a multi-stage RF bunching system [26], producing $\sim 1\text{--}2$ ps bunches. Replacing it with an RF photoinjector enables direct generation of 10 ps bunches in single-bunch operation, with the significantly improved transverse beam quality and precise control over the charge and transverse profile – critical prerequisites for producing structured quantum states.

In this work, we present beam-dynamics simulations of the bunch generation and acceleration in the JINR photoinjector using realistic field maps. We demonstrate the implementation of a Carlsten-type emittance-compensation scheme. Although the emittance does not decrease by an order of magnitude, the solenoidal lens stabilizes the transverse emittance at a low value and suppresses RF-induced phase-space distortions, establishing a robust operating point for subsequent vortex-beam experiments.

We also investigate the quantum evolution of the single-electron Laguerre–Gaussian (LG) wave packets with different OAM values, up to $\ell = 64\hbar$, accelerated in the same realistic DC and RF fields. We find that quantum transverse spreading in both accelerating field configurations is strongly suppressed compared with free-space drift, due to the rapid increase of the longitudinal momentum. This suppression enables realistic estimates of the transverse coherence length of electron wave packets in the photogun under experimentally achievable conditions.

The single-electron regime is justified by the planned experimental capability of operating at ultralow bunch charges approaching the quasi-single-electron limit. Collective effects such as Coulomb repulsion and decoherence are not included in this first study; thus the results represent an upper bound on coherence and OAM-structure preservation during acceleration.

2 Test bench design

The RF photoinjector test bench under construction at JINR is based on an S-band 1.5-cell RF photogun and a high-power UV drive laser. The assembled test bench (see Fig. 1) comprises the RF gun, the UV laser transport line, a steering magnet, two solenoids, and a 1.5-m vacuum beamline at $\sim 10^{-9}$ Torr.

The high accelerating field rapidly increases the electron energy, helping preserve beam quality at the earliest stage. Two solenoids – a cathode solenoid near the gun and a downstream focusing solenoid – shape the transverse phase space and control the beam size.

The 1.5-cell S-band RF gun operates in the π -mode at 2856 MHz [27]. Its internal geometry and photocathode placement (see Fig. 2) are optimized for rapid extraction and emittance-compensating beam formation. The UV laser enters through the coaxial channel, which simultaneously serves as the RF coupling element and the electron-beam exit port. The on-axis accelerating field (see Fig. 3) was obtained from CST Microwave Studio eigenmode simulations [28].

Although the gun is designed for up to 6 MW of input RF power, the present test-bench operation is limited to about 3 MW because the cavity is still undergoing RF aging. Thus the 45 MV/m accelerating

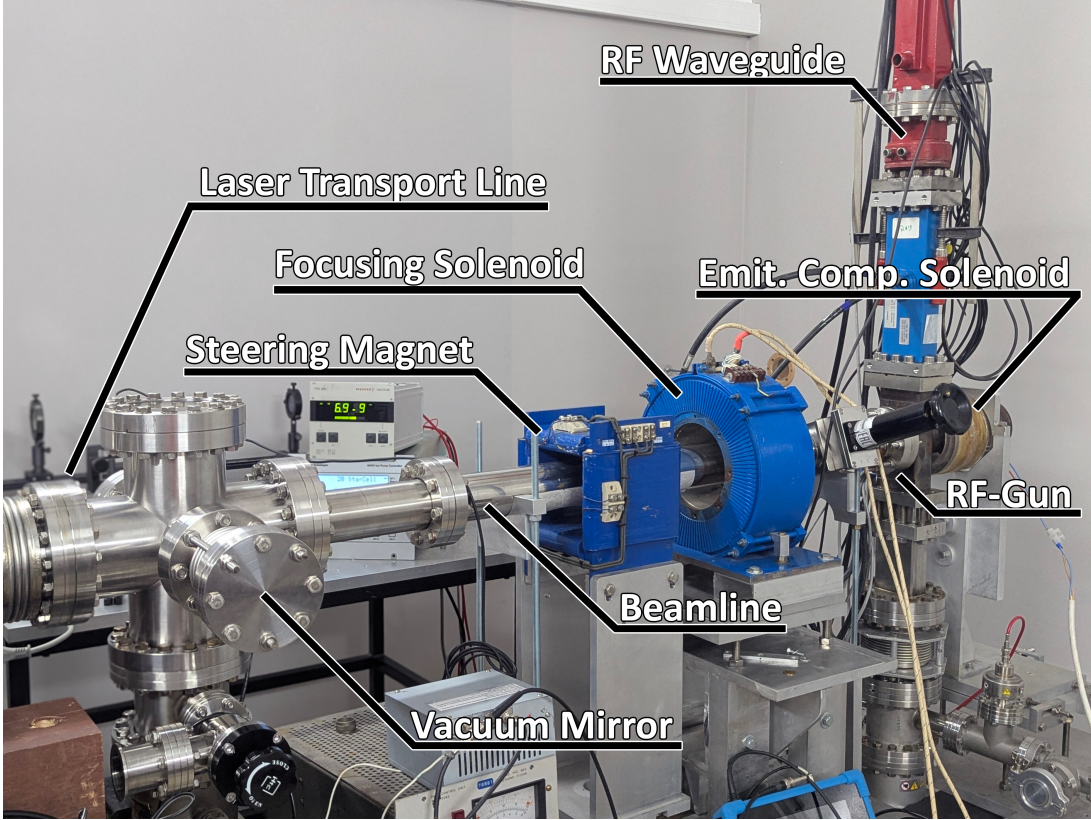


Figure 1: Assembled RF photoinjector test bench during commissioning. The main components are indicated: RF gun, emittance-compensation solenoid, focusing solenoid, steering magnet, RF waveguide, UV laser transport line, vacuum mirror, and beamline.

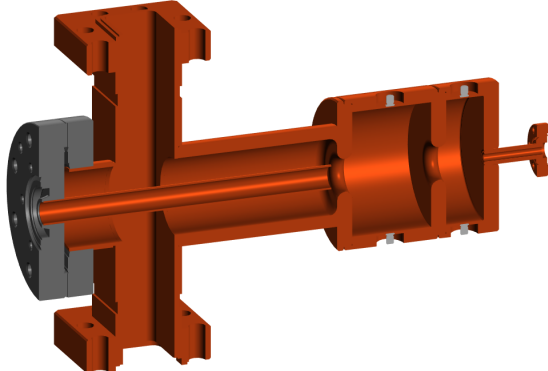


Figure 2: Internal geometry of the S-band RF photogun. The design consists of 1.5 accelerating cells operating in the π -mode at 2856 MHz. The central aperture serves both for laser injection and electron beam extraction.

gradient used in the simulations corresponds to the experimentally achievable field at this commissioning stage.

The UV drive laser is based on a mode-locked ytterbium-doped fiber oscillator at $\lambda = 1047$ nm with a SESAM [29] for pulse shortening; it produces pulses with the duration of $\tau = 10$ ps [19]. Two lamp-pumped Nd:YLF amplifiers raise the pulse energy before sequential generation of the second (KTP) and fourth (BBO) harmonics. A recent upgrade [30] increased the repetition rate to the 71st subharmonic of the RF frequency (40.225 MHz) and introduced synchronized amplifier control, improving UV pulse

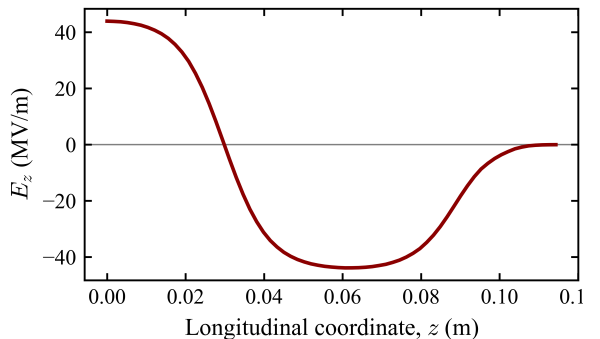


Figure 3: Simulated axial distribution of the accelerating electric field along the beam propagation axis z , obtained using eigenmode analysis in CST Microwave Studio.

stability and achieving 3–4 μJ energies. The laser transport line consists of an atmospheric transport section and a vacuum section delivering the beam to the cathode via a 45° metallic mirror; a 2500-mm focal-length lens produces a 2 mm laser rms beam size on the photocathode.

The emittance-compensation solenoid prototype (see Fig. 4) was manufactured at JINR. It has an inner radius of 100 mm, outer radius of 140 mm, length of 100 mm, and contains 216 copper turns in six layers. The axial field profile, measured with 5-mm resolution at 20 A, is shown in Fig. 5. These measured values are used directly in the beam-dynamics simulations.

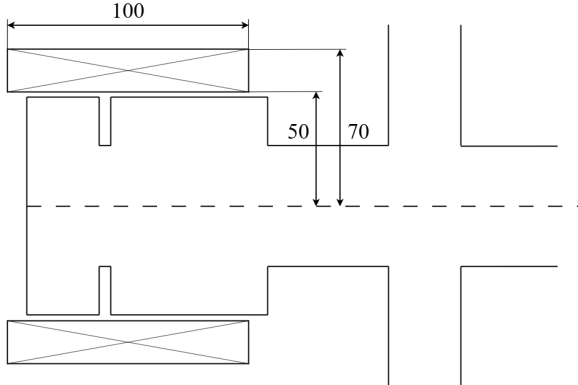


Figure 4: Mechanical layout and positioning of the emittance compensation solenoid along the beamline.

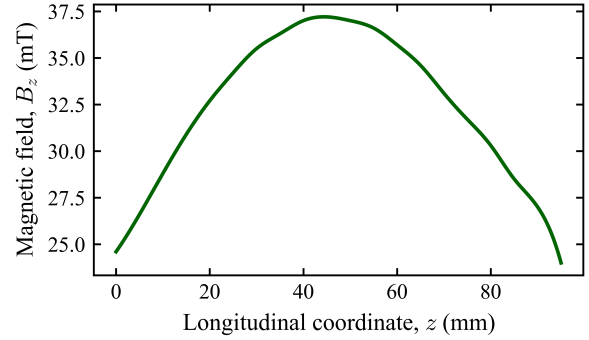


Figure 5: Measured axial magnetic field distribution of the emittance compensation solenoid. The measurement was carried out in 5 mm steps along the z -axis using a magnetic field meter with a coil current of 20 A.

3 Beam dynamics simulation

3.1 Definition of initial parameters

Beam dynamics simulations were carried out with ASTRA [31], which couples a 3D particle-in-cell space-charge solver (in cylindrical symmetry) to high-order Runge–Kutta tracking through RF-cavity and magnetic fields. The key inputs are the bunch charge (from photocathode quantum efficiency and laser energy), mean initial energy and its spread, initial normalized emittance and spatial/momentum distributions, and the RF phase at photoemission.

The initial beam parameters are derived from the properties of the UV drive laser and the copper photocathode. The fourth-harmonic laser operates at $\lambda = 262$ nm, corresponding to a photon energy of 4.74 eV. With typical UV pulse energies of 3 μJ delivered to the vacuum chamber and taking into account the measured transport losses, the number of photons incident on the cathode is of order 4×10^{11} per pulse.

Using a copper photocathode with a quantum efficiency of $QE \sim 10^{-5}$ [32], this yields an emitted charge of approximately

$$Q = 0.63 \text{ pC},$$

which is used as the baseline value in the simulations.

The photoemission model follows the Dowell–Schmerge approach [33], assuming Fermi–Dirac statistics and Gaussian spatial distributions. For an effective copper work function of $\phi_{\text{eff}} = 4.3$ eV [34], the resulting mean kinetic energy and energy spread of emitted electrons lie in the sub-eV range, consistent with standard metallic photocathodes. With the UV laser rms beam size set to $\sigma_{x,y} = 2$ mm (equal to the initial RMS beam size), the corresponding intrinsic normalized emittance is

$$\varepsilon_{n,x,y} = 1.07 \pi \cdot \text{mm} \cdot \text{mrad},$$

which defines the initial phase-space conditions used for the beam-dynamics simulations.

A simulated RF-phase scan was performed to determine the optimal injection phase. Figure 6 shows the mean beam energy as a function of the initial RF phase φ_0 . Maximum acceleration is achieved near $\varphi_0 \approx 180^\circ$, with a phase tolerance of about $\pm 1^\circ$.

The phase scan of the normalized transverse emittance (see Fig. 7) shows a pronounced overall increase with injection phase in the explored interval. This behaviour is primarily determined by the intrinsic field

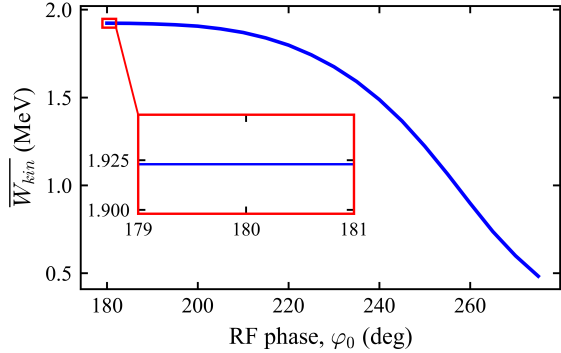


Figure 6: Simulated dependence of the mean beam energy on the injection RF phase φ_0 . Maximum acceleration is obtained near $\varphi_0 \approx 180^\circ$, consistent with π -mode operation of the RF gun.

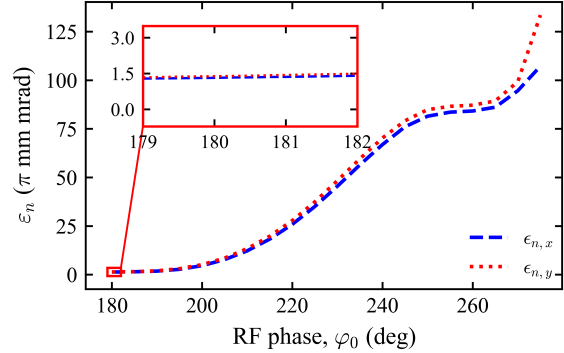


Figure 7: Simulated dependence of the final normalized transverse emittance on the injection RF phase φ_0 . The operational working region $\varphi_0 \approx 180^\circ$.

structure of the 1.5-cell S-band RF gun operating in the π -mode: the axial electric field has a node close to the cathode plane, so the extraction field falls rapidly as the phase approaches the zero crossing.

For realistic simulations, apertures corresponding to the internal structure of the RF gun were added (see Fig. 2): two apertures with an inner diameter of $d = 21.8$ mm and a length of 10 mm, simulating the resonator cell walls, as well as an aperture with an inner diameter of $d = 14$ mm and a length of 190 mm, simulating the coaxial input for impedance matching and RF power injection into the resonator cells. Simulations without the external solenoidal field demonstrate that most of the particles from the generated beam are lost within the first 25 cm from the cathode inside the coaxial input.

At the present low bunch charge (0.63 pC), the emittance is thus governed mainly by RF-induced transverse correlations imposed by the cavity geometry and mode structure, rather than by space-charge forces. This field configuration explains the observed monotonic phase dependence of the emittance. The operational working point of the test bench, chosen to maximize the energy gain under the available RF gradient, lies at $\varphi_0 \approx 180^\circ$. In this region the field on the cathode is not maximal, which inevitably increases the extraction-induced emittance, but it provides the highest attainable beam energy at the current stage of commissioning. The results of this scan define the initial parameters used in the subsequent beam-dynamics simulations (Table 1).

Table 1: Initial parameters for beam dynamics simulations.

Parameter	Value
Photon energy	4.74 eV
Work function (Cu)	4.3 eV
Mean kinetic energy	0.29 eV
RMS energy spread	0.10 eV
RMS beam size at cathode	2.0 mm
Normalized emittance	$1.07 \pi \text{ mm mrad}$
Number of emitted electrons	3.95×10^6
Bunch charge	0.63 pC
Optimal RF phase	180°
Total beamline length	1.568 m

3.2 Beam dynamics without emittance compensation

This process is identical for both simulation scenarios, with and without the emittance-compensating solenoid, as it depends solely on the amplitude of the RF field and the proper injection phase, and is independent of external magnetic fields.

Fig. 8 shows the simulated mean kinetic energy of the bunch along the RF photogun beamline. A two-peak structure arises from the axial field in the S-band RF photogun, with rapid acceleration to $\bar{W}_{\text{kin}} = 1.9$ MeV at the gun exit, followed by a plateau. High-gradient injection quickly suppresses space-charge driven emittance growth once $\gamma \gg 1$, although early nonlinear distortions remain significant. Longitudinally,

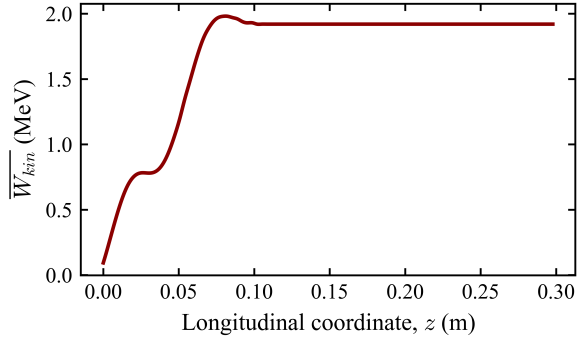


Figure 8: Simulated mean kinetic energy of the electron bunch along the beamline. The beam rapidly reaches relativistic energies in the RF photogun, exiting with mean energy $\overline{W_{kin}} = 1.9$ MeV.

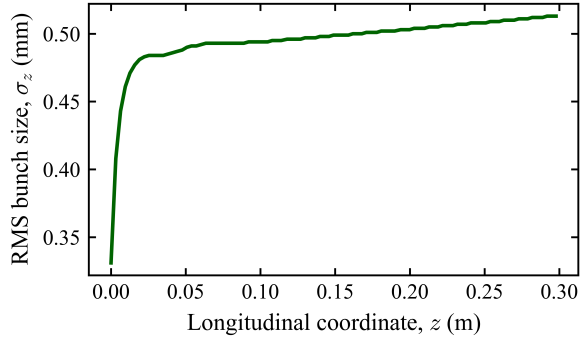


Figure 9: Simulated RMS bunch length σ_z along the beamline. Rapid longitudinal expansion occurs during RF photogun acceleration, followed by gradual growth from energy spread and residual space-charge effects.

the bunch length σ_z (see Fig. 9) increases rapidly during acceleration due to the velocity–energy correlation, as faster electrons at the head outpace slower ones at the tail; beyond the cavity, the expansion continues more gradually under residual space-charge forces.

The simulated energy evolution is defined by the presently available RF power. Consequently, the accelerating gradient is reduced to 45 MV/m, resulting in a final kinetic energy of 1.9 MeV in Fig. 8. The reduced gradient also increases the relative importance of space-charge forces during the first few millimeters after the emission.

Transversely, the beam expands symmetrically in x and y (see Fig. 10) from 2 mm to nearly 5.5 mm in the absence of external focusing. At the present low bunch charge (0.63 pC) and relatively large emission area, the space-charge forces are moderate and contribute mainly to the divergence of the transverse envelope. The evolution of the normalized emittance, however, is dominated by correlated distortions from the transverse RF fields of the 1.5-cell π -mode gun, rather than by space charge.

As shown in Fig. 11, the emittance remains near $1.5 \pi \cdot \text{mm} \cdot \text{mrad}$ at the cavity exit but exhibits early oscillations characteristic of RF-induced correlations. These oscillations become particularly relevant when a solenoidal field is introduced, since the RF–solenoid coupling modifies their cancellation. Without external focusing, the beam size diverges rapidly and RF-induced emittance growth cannot be mitigated, motivating the use of a compensation solenoid in the following section.

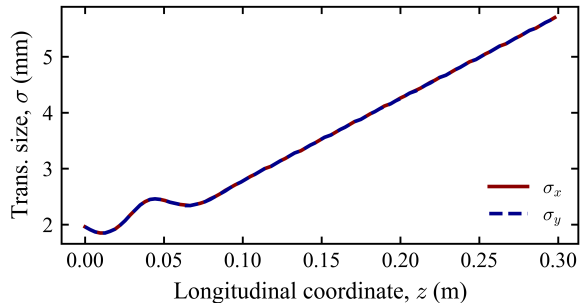


Figure 10: Simulated RMS transverse beam sizes σ_x and σ_y along the beamline, showing symmetric growth from 2 mm to nearly 5.5 mm.

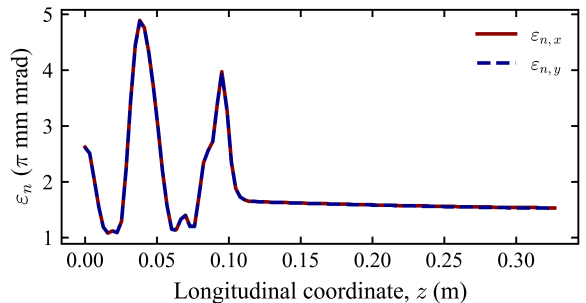


Figure 11: Simulated evolution of the normalized transverse emittance along the beamline. After initial RF-induced oscillations inside the 1.5-cell gun, the emittance remains approximately constant at the cavity exit and subsequently increases due to nonlinear RF-field–induced transverse phase-space distortions.

Because the space-charge effects are weak in this regime, they can be neglected in the subsequent analysis. This is particularly important for the quantum-mechanical considerations in Sec. 4, since the small Coulomb forces do not significantly perturb the phase structure or the orbital-angular-momentum content of the evolving electron wave packet.

3.3 Emittance compensation using a solenoidal lens

A solenoidal lens is installed near the cathode (see Fig. 4) to counteract early nonlinear space-charge effects. The on-axis field profile used in the simulations (see Fig. 5) was optimized via iterative scans, yielding a peak of $B_z = 125$ mT at $z = 85$ mm downstream of the photocathode.

Fig. 12 shows the resulting RMS transverse beam size. Immediately after the RF cavities, the solenoid collimates the envelope, stabilizing $\sigma_{x,y}$ along the beamline. The normalized emittance (see Fig. 13) initially rises due to the non-zero solenoidal field at the cathode, which imparts extrinsic angular momentum onto the beam. In addition, the combination of the solenoidal field with the transverse RF fields of the 1.5-cell π -mode gun modifies the evolution of the transverse phase space and suppresses the natural cancellation of RF-induced correlations that occurs in the zero-solenoid case [35].

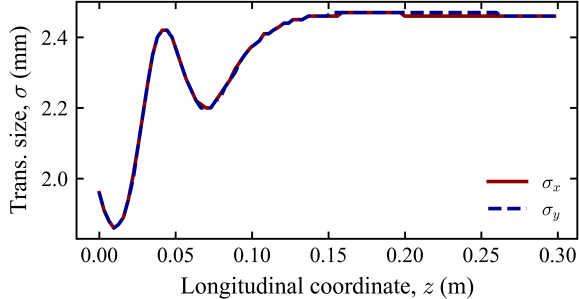


Figure 12: Simulated RMS transverse beam size along the beamline with the compensation solenoid. The size stabilizes soon after the RF cavities, indicating effective collimation.

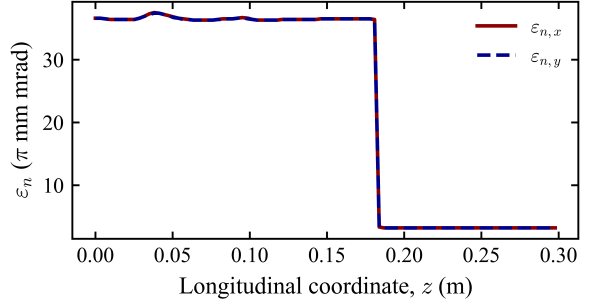


Figure 13: Simulated normalized transverse emittance along the beamline with solenoid compensation. Stabilizes near $3.2 \pi \cdot \text{mm} \cdot \text{mrad}$ downstream.

To verify that the cathode solenoid has been properly designed and that its magnetic field provides effective beam stabilization, we performed additional particle-tracking simulations through the RF gun (see Fig. 16). Figure 14 shows the transverse particle distribution at the exit of the accelerating structure. The rms transverse spread does not exceed 5 mm, which allows the beam to be safely transported through the 14-mm-diameter coaxial aperture.

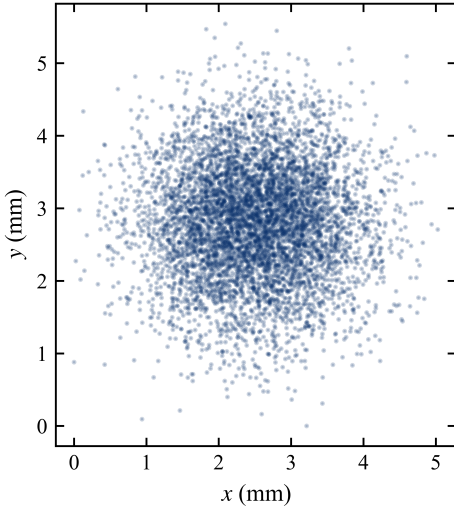


Figure 14: Simulated transverse particle distribution at the exit of the RF accelerating structure in the presence of the cathode solenoid. The transverse spread of the beam remains within 5 mm, allowing transmission through the 14-mm-diameter coaxial aperture.

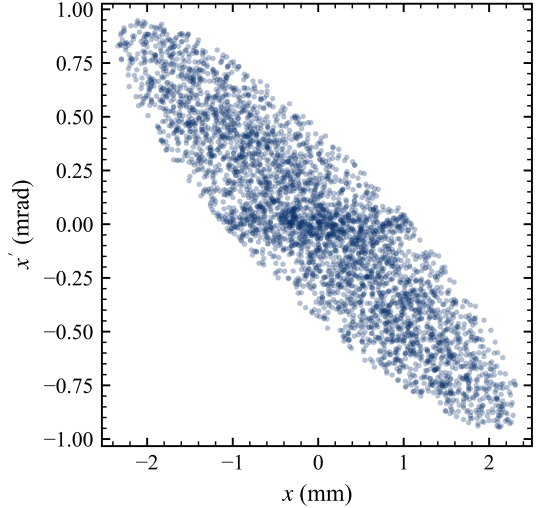


Figure 15: Simulated transverse phase space of the electron beam at the RF-gun exit. The $x-x'$ projection exhibits an approximately ideal phase-space ellipse, indicating stable beam formation.

In addition, Fig. 15 shows the two-dimensional transverse phase space of the beam. The $x-x'$ projection exhibits an almost ideal phase-space ellipse, indicating stable transverse dynamics and good beam quality,

even at relatively large transverse emittance values. Since the simulation corresponds to on-axis beam transport through the solenoid, an identical phase-space distribution is expected in the y - y' plane.

Figure 16 presents the particle trajectories along the beamline. Most particles are transmitted through the RF gun to its exit. A small fraction of electrons remains near the photocathode region, while another fraction is partially lost at the coaxial aperture. Nevertheless, the total beam loss does not exceed 13%, which indicates a satisfactory operating regime of the cathode solenoid and confirms its effectiveness for beam confinement.

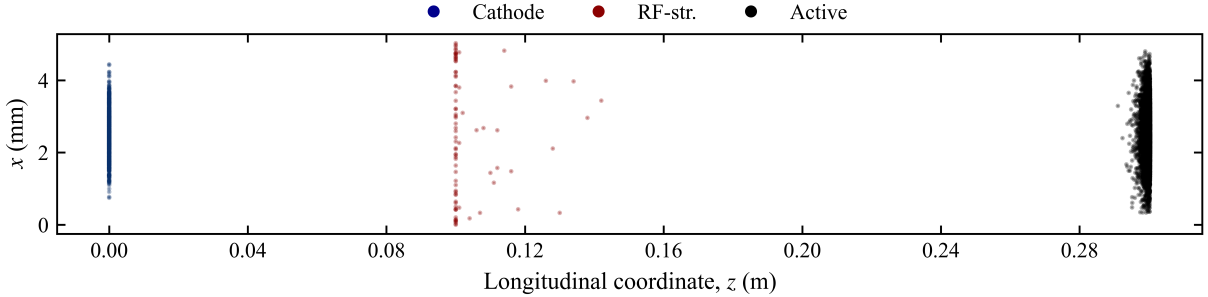


Figure 16: Simulated particle trajectories along the RF photogun beamline with the cathode solenoid. Black dots denote transmitted (active) particles, blue dots correspond to particles remaining in the photocathode region, and red dots indicate particles lost inside the RF structure.

4 Quantum beam dynamics

The classical beam dynamics simulations presented above demonstrates that the photoinjector can operate in a regime of low bunch charge and correspondingly weak space-charge forces, yielding a stable, low-emittance beam with minimal RF-induced phase-space distortions. This establishes that the test bench is capable of producing high-quality electron wave packets under realistic operating conditions. In this regime, it becomes essential to evaluate whether structured quantum states – specifically, vortex electrons – can be generated and accelerated while preserving their spatial coherence and OAM content. Motivated by the experimentally accessible values of orbital angular momentum that can be imparted by our UV vortex optics, we now turn to the quantum description of single-electron Laguerre–Gaussian states in the RF fields of the photoinjector.

4.1 Vortex electrons

In general, a vortex electron beam is a free-electron state whose wave function can be represented in terms of an LG mode, an exact non-stationary solution of the Schrödinger equation and a close analogue of optical vortex modes [36]. Its transverse wave function can be written as [3]

$$\begin{aligned} \psi_{\ell,n}(\rho, t) = & N \frac{\rho^{|\ell|}}{(\sigma_{\perp}(t))^{|\ell|+1}} L_n^{|\ell|} \left(\frac{\rho^2}{(\sigma_{\perp}(t))^2} \right) \\ & \times \exp \left[i\ell\phi_r - i(2n + |\ell| + 1) \arctan \left(\frac{t}{t_d} \right) \right. \\ & \left. - \frac{\rho^2}{2(\sigma_{\perp}(t))^2} \left(1 - i \frac{t}{t_d} \right) \right] \end{aligned} \quad (1)$$

where the normalization constant N is chosen such that

$$\int d^2x |\psi_{\ell,n}(\rho, t)|^2 = 1. \quad (2)$$

Here, $\ell = 0, \pm 1, \pm 2, \dots$, is the OAM in units of \hbar , $n = 0, 1, 2, \dots$, is the radial quantum number, L_n^{ℓ} denotes the generalized Laguerre polynomial, $\sigma_{\perp}(t)$ is the transverse beam size of the fundamental LG mode: for

$n = \ell = 0$, and t_d is the characteristic diffraction time. It is important to note that the azimuthal phase factor $\exp(i\ell\phi_r)$ makes the state an eigenfunction of the OAM operator,

$$\hat{L}_z \psi_{\ell,n} = -i\hbar \frac{\partial}{\partial \phi_r} \psi_{\ell,n} = \ell\hbar \psi_{\ell,n},$$

and it is the defining feature of vortex beams: it produces the characteristic helical phase front and ensures that each electron carries an orbital momentum projection $\ell\hbar$ with respect to the propagation axis.

One mechanism for generating vortex electrons in an RF photoinjector at an accelerator facility is laser-driven emission using structured light. Theory shows that an atom placed on the axis of an optical vortex transfers a well-defined OAM projection to the emitted electron, and this behaviour persists for ensembles [16, 17]. Alternative schemes based on electron diffraction [5, 6, 7] are impractical in such setups.

4.2 Quantum evolution of a single-electron wave packet in the accelerating field

To analyze the generation of relativistic vortex electrons carrying OAM, we follow the quantum evolution of a single-electron wave packet during acceleration. As a convenient observable we consider the mean-squared transverse radius $\langle \rho^2 \rangle(\langle z \rangle)$, which for an LG wave packet is related to the transverse rms width via [3]

$$\langle \rho^2 \rangle(\langle z \rangle) = \sigma_{\perp}^2(\langle z \rangle) (2n + |\ell| + 1). \quad (3)$$

Throughout this section, the angular brackets denote quantum expectation values over the single-electron state. We compare three representative cases:

1. Free-space propagation over the RF photogun length;
2. Acceleration in a uniform DC electric field, corresponding to a simplified DC-gun model;
3. Acceleration in the realistic standing-wave RF field of the photoinjector.

The general law of transverse quantum spreading for free (field-less) wave packets [3] can be written either as a function of the mean propagation distance $\langle z \rangle$ or of the corresponding time of flight $t(\langle z \rangle)$:

$$\langle \rho^2 \rangle(\langle z \rangle) = \langle \rho^2 \rangle(0) \left(1 + \frac{\langle z \rangle^2}{z_R^2} \right) = \langle \rho^2 \rangle(0) \left(1 + \frac{t^2(\langle z \rangle)}{t_d^2} \right). \quad (4)$$

Here z_R is the Rayleigh length and t_d is the diffraction time [3],

$$z_R = \frac{2\pi}{M} \frac{\langle \rho^2 \rangle(0)}{\lambda_{\text{dB}}}, \quad t_d = \frac{m \langle \rho^2 \rangle(0)}{\hbar M}, \quad (5)$$

where $M = 2n + |\ell| + 1$ is the beam-quality factor of the packet and λ_{dB} is the de Broglie wavelength. Note that Eqs. (4) and (5) depend on the quantum numbers (n, ℓ) only through the combination M and the initial second moment $\langle \rho^2 \rangle(0)$; therefore the same transverse spreading law applies to any coherent single-electron state, not only to the LG modes, provided that they share the same initial rms transverse radius.

In the far-field regime, $\langle z \rangle \gg z_R$, Eq. (4) reduces to a simple relation, often referred to as a van Cittert–Zernike–type theorem [3], between the measured packet width at the detector and the initial width near the source,

$$\sqrt{\langle \rho^2 \rangle(0)} = \frac{\langle z \rangle \lambda_{\text{dB}}}{2\pi \sqrt{\langle \rho^2 \rangle(\langle z \rangle)}} M. \quad (6)$$

In the intermediate (Fresnel) regime the transverse width obeys

$$\begin{aligned} \sqrt{\langle \rho^2 \rangle(\langle z \rangle)} &= \frac{\langle z \rangle \lambda_{\text{dB}}}{2\pi \sqrt{\langle \rho^2 \rangle(0)}} M \\ &\times \left[1 + \frac{1}{2} \left(\frac{2\pi \langle \rho^2 \rangle(0)}{\langle z \rangle \lambda_{\text{dB}}} \frac{1}{M} \right)^2 \right]. \end{aligned} \quad (7)$$

For an initial rms transverse radius $\sqrt{\langle \rho^2 \rangle(0)} = 1$ nm, typical for an electron packet near the emission region [3, 37], with $n = 3$ and $\ell = 1$ (OAM = $\ell\hbar$) and a drift length of 30 cm, Eq. (4) predicts free-space spreading to an rms transverse width of about 0.8 m for an initial kinetic energy of 0.3 eV. Next, we include acceleration.

Uniform DC acceleration. In a static electric field $\mathbf{E} = E\hat{\mathbf{z}}$ with a scalar potential $A^0 = -Ez$ and $\mathbf{A} = 0$, the Hamiltonian separates as

$$\hat{H} = \frac{p_x^2 + p_y^2}{2m} + \left(\frac{p_z^2}{2m} + qEz \right) \equiv \hat{H}_\perp + \hat{H}_z, \quad (8)$$

so that $[\hat{H}_\perp, \hat{H}_z] = [\rho^2, \hat{H}_z] = 0$. The transverse quantum evolution is therefore *identical* to free space; the only modification arises through the shortened time of flight to a given longitudinal coordinate z . Using $\varepsilon(z) = \varepsilon_0 + qEz$ and $p(z) = \sqrt{\varepsilon(z)^2 - m^2c^4}/c$, one finds

$$t(z) = \frac{p(z) - p_0}{qE}, \quad (9)$$

where for acceleration of electrons along $+z$ one has $E < 0$ and hence $qE > 0$, so that $t(z) > 0$. The transverse second moment at a fixed plane z is then obtained by evaluating Eq. (4) at this $t(z)$. For typical DC-gun this results in a ~ 550 -fold reduction of the final transverse width compared to free-space propagation (see Fig. 17), in good agreement with recent relativistic calculations [38].

RF standing-wave acceleration. In the S-band photoinjector electrons are accelerated in a standing-wave RF field. Along the axis, where the packet propagates, the longitudinal electric field can be written as [39, 40, 41]

$$E_z(z) = E_{z0} \sin\left(\omega \frac{z}{v} + \phi\right), \quad (10)$$

where E_{z0} is the peak amplitude, ω is the RF angular frequency, and ϕ is the injection phase. The corresponding kinetic-energy gain over an accelerating gap of length d is

$$\Delta E_{\text{kin}} = eE_{z0} \int_{-d/2}^{d/2} \cos\left(\omega \frac{z}{v} + \phi\right) dz, \quad (11)$$

which accounts for the phase-dependent acceleration experienced by particles with finite longitudinal extent and underlies the development of a velocity–energy correlation during bunching. The on-axis energy profile $K(z)$ used below is obtained from the simulated field map.

Hamiltonian structure. In the TM₀₁₀ standing-wave mode the on-axis electromagnetic field is predominantly longitudinal. Near the axis the field admits the expansions

$$E_z(\rho, z, t) = E_z(0, z, t) + \mathcal{O}(\rho^2), \quad (12)$$

$$B_\varphi(\rho, z, t) = \mathcal{O}(\rho/R_{\text{cav}}), \quad (13)$$

where R_{cav} is the cavity radius. For a nanometer-scale packet one has $\rho/R_{\text{cav}} \lesssim 10^{-8}$, so that $|qvB_\varphi|/|qE_z| \ll 10^{-7}$ and transverse magnetic forces are negligible.

In a gauge with $A^0 = 0$ and a purely longitudinal vector potential $A_z(z, t)$ satisfying $E_z = -\partial_t A_z$, the single-particle Hamiltonian takes the form

$$\hat{H}(t) = \frac{p_x^2 + p_y^2}{2m} + \frac{[p_z - qA_z(z, t)]^2}{2m} \equiv \hat{H}_\perp + \hat{H}_z(t), \quad (14)$$

and, because A_z depends only on z and t ,

$$[\hat{H}_\perp, \hat{H}_z(t)] = 0, \quad [\rho^2, \hat{H}_z(t)] = 0, \quad (15)$$

up to corrections of order $(\rho/R_{\text{cav}})^2$. Thus the transverse dynamics *remains effectively free*, as in the DC case, and the RF field enters only through the longitudinal kinematics.

Longitudinal evolution and time-of-flight. The kinetic energy satisfies

$$K(z) = K_0 + \Delta E_{\text{kin}}(z), \quad \gamma(z) = 1 + \frac{K(z)}{mc^2}, \quad (16)$$

and the local velocity is $\beta(z) = \sqrt{1 - \gamma(z)^{-2}}$. The flight time to a plane at z follows from

$$t(z) = \int_0^z \frac{dz'}{\beta(z') c}. \quad (17)$$

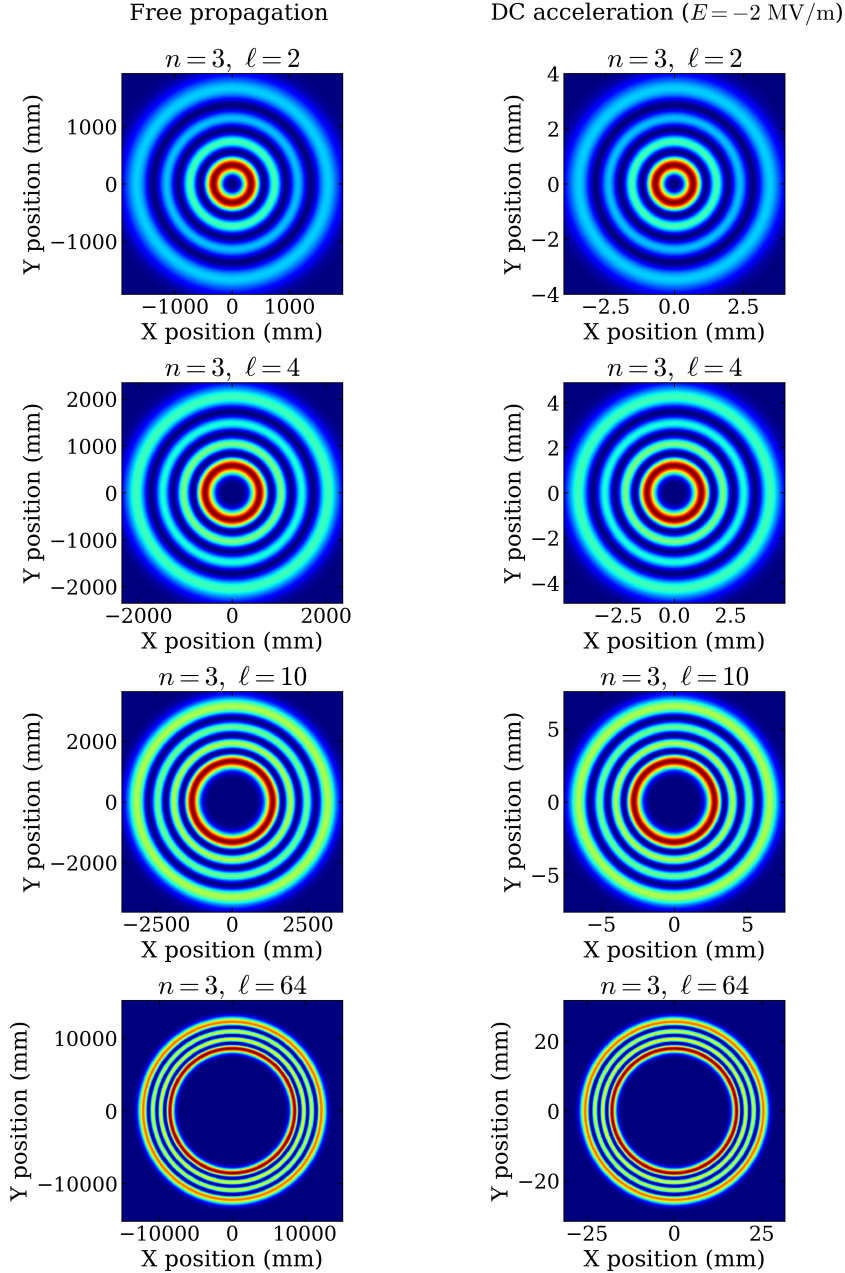


Figure 17: Transverse intensity distributions of the LG wave packets ($n = 3$, $\ell = 2, 4, 10, 64$) with the initial rms transverse radius $\sqrt{\langle \rho^2 \rangle(0)} = 1$ nm and initial kinetic energy $K_0 = 0.39$ eV after 30 cm of propagation. Left column: free-space propagation. Right column: acceleration in a uniform DC field with $E = -2$ MV/m. The normalized maps $|\psi(x, y)|^2$ at the observation plane illustrate the strong suppression of transverse spreading under DC acceleration while preserving the characteristic ring structure of the LG modes.

For the photoinjector parameters used in this work, the resulting relativistic velocity profile reduces the time of flight to the exit plane by almost three orders of magnitude compared to free-space propagation. In the regime $t \gg t_d$, where the transverse width obeys $\sigma_\perp(t) \propto t$, this kinematic shortening leads to an ~ 900 -fold suppression of the transverse rms size compared to the free electron at $z = 30$ cm, as shown in Fig. 18. Importantly, similar suppression of quantum spreading persists for all other parameter sets explored in this work, indicating that strong reduction of transverse spreading is a robust feature of relativistic acceleration rather than a special property of the specific cases illustrated in Figs. 18–17.

These propagation laws, derived for single-particle packets without accounting for collective effects, can be directly applied to structured vortex beams. This provides guidance for preserving spatial coherence and OAM content during beam transport and acceleration. By understanding and controlling this fundamental quantum spreading, photoinjector designs can be optimized to maintain the quality and characteristic

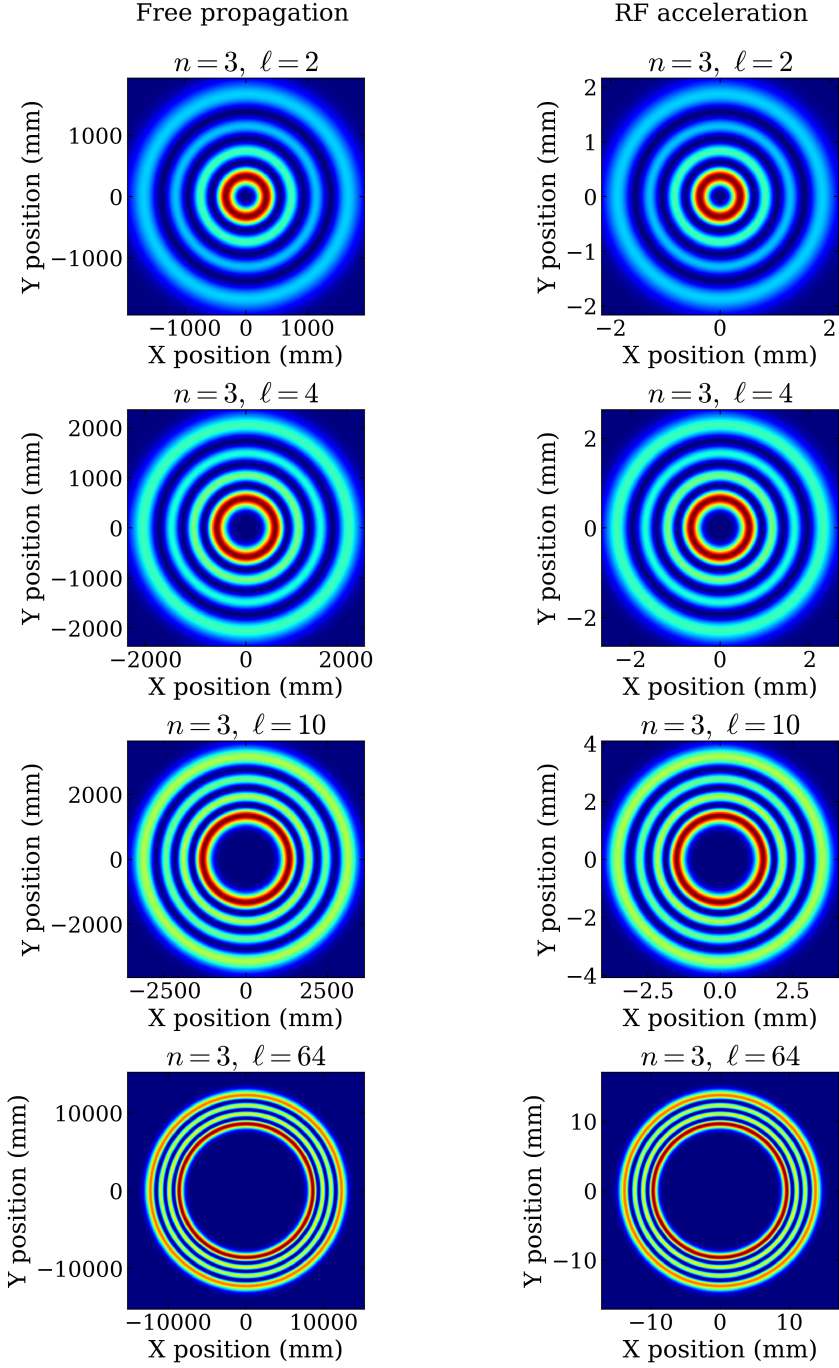


Figure 18: Transverse intensity distributions of the LG wave packets ($n = 3$, $\ell = 2, 4, 10, 64$) with the initial rms transverse radius $\sqrt{\langle \rho^2 \rangle(0)} = 1$ nm and initial kinetic energy $K_0 = 0.39$ eV at $z = 30$ cm for free-space propagation (left) and acceleration in the standing-wave RF field of the S-band photogun (right). The normalized maps $|\psi(x, y)|^2$ demonstrate the strong suppression of transverse spreading during RF acceleration while preserving the characteristic LG ring structure for all OAM values.

properties of the vortex beams throughout the early acceleration stages.

5 Conclusions

We have performed classical and quantum beam-dynamics simulations of the S-band RF photoinjector test bench now being commissioned at JINR. Using realistic electromagnetic field maps and ASTRA tracking, we have showed that the injector can operate in a stable ultralow-charge regime ($Q \approx 0.63$ pC), where space-charge forces are weak and the emittance evolution is dominated by RF-induced correlations.

Under these conditions, a Carlsten-type emittance-compensation scheme was implemented and optimized. Although the solenoid does not reduce the emittance below its intrinsic value, it suppresses RF-driven phase-space distortions and provides a reproducible operating point with a final normalized emittance of $\approx 3.2 \pi \cdot \text{mm} \cdot \text{mrad}$.

The low-charge operating regime has enabled a quantum-mechanical analysis of single-electron states. We have studied the evolution of Laguerre–Gaussian wave packets with the realistic OAM values under three propagation scenarios: free drift, acceleration in a uniform DC field, and acceleration in the standing-wave RF field of the S-band gun. In both accelerating cases, the rapid growth of electron momentum has substantially suppressed transverse spreading compared to free-space propagation, while preserving the characteristic radial structure of the OAM-carrying states.

Overall, the simulations show that the present injector configuration satisfies the beam-quality requirements for experiments on the photoemission-driven generation and acceleration of vortex electrons in the MeV energy range. The photoinjector has been assembled, and the first photoemitted electron beam has been produced. Commissioning of the RF gun is ongoing, with work underway to reach the design input power of 6 MW. In parallel, a phase-locking system for synchronizing the UV laser pulses with the RF field is being developed. All preparations for experiments on photoemission-based generation of relativistic vortex electrons have been completed: diffractive optical elements for producing ultraviolet twisted light beams with orbital angular momentum up to $\ell = 64\hbar$ have been fabricated and tested. Future studies will extend the present modelling by including collective interactions and decoherence mechanisms to obtain a complete description of structured electron beams under realistic experimental conditions. The check of the electron beams vorticity can be made by diffraction on a triangle aperture, as has been discussed in Ref. [42].

Acknowledgments

The authors express their gratitude to A.V. Vukolov, M.V. Shevelev, and G.K. Sizikh for their significant assistance in developing the beam emittance diagnostics. We also thank E.A. Yakushev, V.V. Glagolev, D. V. Naumov, A.S. Zhemchugov, and the management of the Laboratory of Nuclear Problems for supporting the project on behalf of JINR. Special thanks are due to K.V. Cherepanov and N.E. Sheremet for their help with quantum dynamics calculations, and to S.S. Baturin for valuable consultations.

This study was supported by the Russian Science Foundation (Project No. 23-62-10026) [43].

References

- [1] B. A. Knyazev, V. G. Serbo, Beams of photons with nonzero orbital angular momentum projection: new results, *Phys. Usp.* 61 (5) (2018) 449–479. [doi:10.3367/UFNe.2018.02.038306](https://doi.org/10.3367/UFNe.2018.02.038306).
- [2] K. Bliokh, I. Ivanov, G. Guzzinati, L. Clark, R. Van Boxem, A. Béché, R. Juchtmans, M. Alonso, P. Schattschneider, F. Nori, J. Verbeeck, Theory and applications of free-electron vortex states, *Physics Reports* 690 (2017) 1–70, theory and applications of free-electron vortex states. [doi:https://doi.org/10.1016/j.physrep.2017.05.006](https://doi.org/10.1016/j.physrep.2017.05.006).
- [3] D. Karlovets, Vortex particles in axially symmetric fields and applications of the quantum busch theorem, *New Journal of Physics* 23 (3) (2021) 033048. [doi:10.1088/1367-2630/abeacc](https://doi.org/10.1088/1367-2630/abeacc).
- [4] I. P. Ivanov, Promises and challenges of high-energy vortex states collisions, *Progress in Particle and Nuclear Physics* 127 (2022) 103987. [doi:https://doi.org/10.1016/j.ppnp.2022.103987](https://doi.org/10.1016/j.ppnp.2022.103987).
- [5] M. Uchida, A. Tonomura, Generation of electron beams carrying orbital angular momentum, *Nature* 464 (2010) 737—739. [doi:10.1038/nature08904](https://doi.org/10.1038/nature08904).
- [6] J. Verbeeck, H. Tian, P. Schattschneider, Production and application of electron vortex beams, *Nature* 467 (2010) 301—304. [doi:10.1038/nature09366](https://doi.org/10.1038/nature09366).
- [7] A. Blackburn, J. Loudon, Vortex beam production and contrast enhancement from a magnetic spiral phase plate, *Ultramicroscopy* 136 (2014) 127–143. [doi:https://doi.org/10.1016/j.ultramic.2013.08.009](https://doi.org/10.1016/j.ultramic.2013.08.009).

[8] P. Schattschneider, B. Schaffer, I. Ennen, J. Verbeeck, Mapping spin-polarized transitions with atomic resolution, *Phys. Rev. B* 85 (2012) 134422. [doi:10.1103/PhysRevB.85.134422](https://doi.org/10.1103/PhysRevB.85.134422).

[9] Y. Wu, L. Ji, X. Geng, Q. Yu, N. Wang, B. Feng, Z. Guo, W. Wang, C. Qin, X. Yan, L. Zhang, J. Thomas, A. Hützen, M. Büscher, T. P. Rakitzis, A. Pukhov, B. Shen, R. Li, Polarized electron-beam acceleration driven by vortex laser pulses, *New Journal of Physics* 21 (7) (2019) 073052. [doi:10.1088/1367-2630/ab2fd7](https://doi.org/10.1088/1367-2630/ab2fd7).

[10] F. An, D. Bai, H. Cai, S. Chen, X. Chen, H. Duyang, L. Gao, S. Ge, J. He, J. Huang, Z. Huang, I. Ivanov, C. Ji, H. Jia, J. Jiang, X. Kang, S.-B. Kim, C. Kong, W. Kou, Q. Li, Q. Li, J. Liao, J. Ling, C.-E. Liu, X. Ma, H. Qiu, J. Tang, R. Wang, W. Wen, J. Wu, J. Xiao, X. Xiao, Y. Xu, W. Yang, X. Yang, J. Yao, Y. Yuan, M. Zaiba, P. Zhang, S. Zhang, S. Zhao, L. Zou, High-precision physics experiments at huizhou large-scale scientific facilities, *Chinese Physics Letters* 42 (11) (2025) 110102. [doi:10.1088/0256-307X/42/11/110102](https://doi.org/10.1088/0256-307X/42/11/110102).

[11] V. V. Danilov, et al., *The Concept of Round Colliding Beams*, in: Proc. EPAC'96, no. 5 in European Particle Accelerator Conference, JACoW Publishing, Geneva, Switzerland, 1996, pp. 1149–1151. URL <https://proceedings.jacow.org/e96/PAPERS/MOPL/MOP007L.PDF>

[12] R. Brinkmann, Applications of Flat to Round Beam Transformation for Radiation Sources, in: Proc. EPAC'02, no. 8 in European Particle Accelerator Conference, JACoW Publishing, Geneva, Switzerland, 2007, pp. 653–655. [doi:doi.org/10.3204/PUBDB-2016-04008](https://doi.org/10.3204/PUBDB-2016-04008).

[13] Y.-E. Sun, P. Piot, K.-J. Kim, N. Barov, S. Lidia, J. Santucci, R. Tikhoplav, J. Wennerberg, Generation of angular-momentum-dominated electron beams from a photoinjector, *Phys. Rev. ST Accel. Beams* 7 (2004) 123501. [doi:10.1103/PhysRevSTAB.7.123501](https://doi.org/10.1103/PhysRevSTAB.7.123501).

[14] P. Piot, Y.-E. Sun, K.-J. Kim, Photoinjector generation of a flat electron beam with transverse emittance ratio of 100, *Phys. Rev. ST Accel. Beams* 9 (2006) 031001. [doi:10.1103/PhysRevSTAB.9.031001](https://doi.org/10.1103/PhysRevSTAB.9.031001).

[15] K. Floettmann, D. Karlovets, Quantum mechanical formulation of the busch theorem, *Phys. Rev. A* 102 (2020) 043517. [doi:10.1103/PhysRevA.102.043517](https://doi.org/10.1103/PhysRevA.102.043517).

[16] I. I. Pavlov, A. D. Chaikovskaia, D. V. Karlovets, Generation of vortex electrons by atomic photoionization, *Phys. Rev. A* 110 (2024) L031101. [doi:10.1103/PhysRevA.110.L031101](https://doi.org/10.1103/PhysRevA.110.L031101).

[17] P. O. Kazinski, M. V. Mokrinskiy, V. A. Ryakin, Surface photoelectric effect by twisted photons as a source of twisted electrons, *Proceedings of the Royal Society A* 481 (June 2025). [doi:10.1098/rspa.2024.0777](https://doi.org/10.1098/rspa.2024.0777).

[18] D. A. Nikiforov, A. E. Levichev, A. M. Barnyakov, A. V. Andrianov, S. L. Samoilov, Simulation of a radio-frequency photogun for the generation of ultrashort beams, *Electrophysics, Electron and Ion Beams, Physics of Accelerators* 63 (2018) 585–592. [doi:10.1134/S1063784218040163](https://doi.org/10.1134/S1063784218040163).

[19] E. I. Gacheva, A. K. Poteomkin, E. A. Khazanov, V. V. Zelenogorskii, E. V. Katin, G. A. Luchinin, N. I. Balalykin, V. F. Minashkin, M. A. Nozdrin, G. V. Trubnikov, G. D. Shirkov, Laser driver for a photoinjector of an electron linear accelerator (february 2014), *IEEE Journal of Quantum Electronics* 50 (7) (2014) 522–529. [doi:10.1109/JQE.2014.2323472](https://doi.org/10.1109/JQE.2014.2323472).

[20] R. Alley, V. Bharadwaj, J. Clendenin, P. Emma, A. Fisher, J. Frisch, T. Kotseroglou, R. Miller, D. Palmer, J. Schmerge, J. Sheppard, M. Woodley, A. Yeremian, J. Rosenzweig, D. Meyerhofer, L. Serafini, The design for the lcls rf photoinjector, *Nuclear Instruments and Methods in Physics Research Section A: Accelerators, Spectrometers, Detectors and Associated Equipment* 429 (1) (1999) 324–331. [doi:https://doi.org/10.1016/S0168-9002\(99\)00072-8](https://doi.org/10.1016/S0168-9002(99)00072-8).

[21] M. Ferrario, K. Flottmann, T. Limberg, P. Piot, B. Grigorian, Conceptual design of the XFEL photoinjector, 2001. [doi:10.3204/PUBDB-2018-04062](https://doi.org/10.3204/PUBDB-2018-04062).

[22] A. Cahill, A. Fukasawa, J. Rosenzweig, B. Spataro, A. Valloni, L. Failace, *Simulations for the high gradient, low emittance supergun rf photoinjector*, in: *Proceedings of LINAC2014*, Geneva, Switzerland, Vol. 1, 2014, pp. 391–393. URL <https://proceedings.jacow.org/LINAC2014/papers/mopp140.pdf>

[23] A. Giribono, D. Alesini, F. Cardelli, G. Di Raddo, L. Faillace, M. Ferrario, A. Gallo, A. Gizzi, S. Lauciani, A. Liedl, L. Pellegrino, L. Piersanti, C. Vaccarezza, A. Vannozzi, J. Scifo, L. Ficcadenti, G. Castorina, G. Pedrocchi, G. J. Silvi, T. G. Lucas, Dynamics studies of high brightness electron beams in a normal conducting, high repetition rate *c*-band injector, *Phys. Rev. Accel. Beams* 26 (2023) 083402. [doi:10.1103/PhysRevAccelBeams.26.083402](https://doi.org/10.1103/PhysRevAccelBeams.26.083402).

[24] J. L. Maltseva, S. A. Melnikov, I. N. Meshkov, A. S. Sergeev, A. A. Cherevko, Space charge of an electron beam in an electron cooling system, *Physics of Atomic Nuclei* 86 (2023) 2439–2445. [doi:10.1134/S1063778823110285](https://doi.org/10.1134/S1063778823110285).

[25] M. Nozdrin, V. Kobets, M. Acosta, A. Afanasiev, A. Brukva, K. Bunyatov, N. Garanzha, D. Demin, A. Dyatlov, P. Zhuravlev, S. Nadgerieva, A. Skrypnik, A. Stankus, A. Trifonov, A. Ulankin, V. Shabratov, D. Shokin, K. Yunenko, V. Glagolev, *Jinr dlnp linear electron accelerator (linac): Status of the commissioning and outlook*, in: Proc. RuPAC2025, Russian Particle Accelerator Conference, 2025, p. 62.
URL <https://indico.inp.nsk.su/event/131/attachments/1754/2658/RuPAC25-Book-of-Abstracts.pdf>

[26] M. Nozdrin, M. Gostkin, V. Kobets, Y. Samofalova, G. Shirkov, A. Trifonov, K. Yunenko, A. Zhemchugov, Linac-200: A New Electron Test Beam Facility at JINR, in: Proc. IPAC'21, no. 12 in International Particle Accelerator Conference, JACoW Publishing, Geneva, Switzerland, 2021, pp. 2697–2699. [doi:10.18429/JACoW-IPAC2021-WEPAB042](https://doi.org/10.18429/JACoW-IPAC2021-WEPAB042).

[27] Y. Samofalova, A. Barnyakov, V. Kobets, M. Nozdrin, A. Zhemchugov, Design and simulation of an s-band rf photogun for a new injector of the accelerator linac-200 at jinr, in: 27th Russian Particle Accelerator Conference, 2021. [doi:10.18429/JACoW-RuPAC2021-TUPSB44](https://doi.org/10.18429/JACoW-RuPAC2021-TUPSB44).

[28] CST – Computer Simulation Technology, *CST Microwave Studio Workflow & Solver Overview* (2010).
URL <https://www.3ds.com/products/simulia/cst-studio-suite>

[29] U. Keller, K. Weingarten, F. Kartner, D. Kopf, B. Braun, I. Jung, R. Fluck, C. Honninger, N. Matuschek, J. Aus der Au, Semiconductor saturable absorber mirrors (sesam's) for femtosecond to nanosecond pulse generation in solid-state lasers, *IEEE Journal of Selected Topics in Quantum Electronics* 2 (3) (1996) 435–453. [doi:10.1109/2944.571743](https://doi.org/10.1109/2944.571743).

[30] A. Dyatlov, V. Bleko, K. Cherepanov, V. Kobets, M. Martyanov, M. Nozdrin, A. Sergeev, N. Sheremet, A. Zhemchugov, D. Karlovets, Status report on modification of jinr uv laser for generating relativistic vortex electrons, in: 2024 International Conference Laser Optics (ICLO), 2024, pp. 438–438. [doi:10.1109/ICLO59702.2024.10624179](https://doi.org/10.1109/ICLO59702.2024.10624179).

[31] K. Floettmann, *Astra User's Manual*, DESY, Hamburg (2017).
URL https://www.desy.de/~mpyflo/Astra_manual/Astra-Manual_V3.2.pdf

[32] R. Xiang, J. Teichert, Photocathodes for high brightness photo injectors, *Physics Procedia* 77 (2015) 58–65, international Conference on Laser Applications at Accelerators, LA3NET 2015, 25-27 March 2015, Mallorca, Spain. [doi:https://doi.org/10.1016/j.phpro.2015.11.010](https://doi.org/10.1016/j.phpro.2015.11.010).

[33] D. H. Dowell, J. F. Schmerge, Quantum efficiency and thermal emittance of metal photocathodes, *Phys. Rev. ST Accel. Beams* 12 (2009) 074201. [doi:10.1103/PhysRevSTAB.12.074201](https://doi.org/10.1103/PhysRevSTAB.12.074201).

[34] S. Karkare, I. Bazarov, Effects of surface nonuniformities on the mean transverse energy from photocathodes, *Phys. Rev. Appl.* 4 (2015) 024015. [doi:10.1103/PhysRevApplied.4.024015](https://doi.org/10.1103/PhysRevApplied.4.024015).

[35] K. Floettmann, rf-induced beam dynamics in rf guns and accelerating cavities, *Phys. Rev. ST Accel. Beams* 18 (2015) 064801. [doi:10.1103/PhysRevSTAB.18.064801](https://doi.org/10.1103/PhysRevSTAB.18.064801).

[36] L. Allen, M. W. Beijersbergen, R. J. C. Spreeuw, J. P. Woerdman, Orbital angular momentum of light and the transformation of laguerre-gaussian laser modes, *Phys. Rev. A* 45 (1992) 8185–8189. [doi:10.1103/PhysRevA.45.8185](https://doi.org/10.1103/PhysRevA.45.8185).

[37] D. Ehberger, J. Hammer, M. Eisele, M. Krüger, J. Noe, A. Högele, P. Hommelhoff, Highly coherent electron beam from a laser-triggered tungsten needle tip, *Phys. Rev. Lett.* 114 (2015) 227601. [doi:10.1103/PhysRevLett.114.227601](https://doi.org/10.1103/PhysRevLett.114.227601).

- [38] Q. Meng, Z. Huang, X. Liu, W. Ma, Z. Yang, L. Lu, A. J. Silenko, P. Zhang, L. Zou, [Relativistic quantum mechanics of charged vortex particles accelerated in a uniform electric field](#), Phys. Rev. Res. 7 (2025) 043213. [doi:10.1103/z6j7-grs2](#).
URL <https://link.aps.org/doi/10.1103/z6j7-grs2>
- [39] H. Wiedemann, Particle Accelerator Physics, 4th Edition, Springer Cham, 2015. [doi:10.1007/978-3-319-18317-6](#).
- [40] A. W. Chao, Lectures on Accelerator Physics, 1st Edition, World Scientific, 2020. [doi:10.1142/12004](#).
- [41] S. Y. Lee, Accelerator Physics, 4th Edition, World Scientific Publishing Company, 2021. [doi:10.1142/11111](#).
- [42] M. Maksimov, N. Borodin, D. Kargina, D. Naumov, D. Karlovets, Diffraction by circular and triangular apertures as a diagnostic tool of twisted matter waves, Phys. Rev. A (2025) –[doi:10.1103/z2rs-2ryl](#).
- [43] Russian Science Foundation (Project No. 23-62-10026), <https://rscf.ru/en/project/23-62-10026/>.